

Magnetic field extrapolation in active region well comparable with observations in multiple layers

FU YU ^{1,2,3}, JIE ZHAO ^{1,3}, YANG SU ^{1,2}, XIAOSHUAI ZHU ³, YANG GUO ⁴, JINHUA SHEN ⁵ AND HUI LI ^{1,2}

¹Key Laboratory of Dark Matter and Space Astronomy, Purple Mountain Observatory, Chinese Academy of Sciences, Nanjing 210023, People's Republic of China

²School of Astronomy and Space Science, University of Science and Technology of China, Hefei 230026, People's Republic of China

³State Key Laboratory of Space Weather, National Space Science Center, Chinese Academy of Sciences, Beijing, 100190, People's Republic of China

⁴School of Astronomy and Space Science and Key Laboratory for Modern Astronomy and Astrophysics, Nanjing University, Nanjing 210023, People's Republic of China

⁵Xinjiang Astronomical Observatory, CAS, Urumqi, 830011, Peoples Republic of China

(Accepted on 06-Apr-2023 by APJ)

ABSTRACT

Magnetic field extrapolation is a fundamental tool to reconstruct the three-dimensional magnetic field above the solar photosphere. However, the prevalently used force-free field model might not be applicable in the lower atmosphere with non-negligible plasma β , where the crucial process of flux rope formation and evolution could happen. In this work, we perform extrapolation in active region (AR) 12158, based on an recently developed magnetohydrostatic (MHS) method which takes plasma forces into account. By comparing the results with those from the force-free field extrapolation methods, we find that the overall properties, which are characterized by the magnetic free energy and helicity, are roughly the same. The major differences lie in the magnetic configuration and the twist number of magnetic flux rope (MFR). Unlike previous works either obtained sheared arcades or one coherent flux rope, the MHS method derives two sets of MFR, which are highly twisted and slightly coupled. Specifically, the result in the present work is more comparable with the high-resolution observations from the chromosphere, through the transition region to the corona, such as the filament fibrils, pre-eruptive braiding characteristics and the eruptive double-J shaped hot channel. Overall, our work shows that the newly developed MHS method is more promising to reproduce the magnetic fine structures that can well match the observations at multiple layers, and future data-driven simulation based on such extrapolation will benefit in understanding the critical and precise dynamics of flux rope before eruption.

Keywords: Solar photosphere (1518); Solar chromosphere (1479); Solar corona (1483); Solar extreme ultraviolet emission (1493); Solar active regions (1974); Solar magnetic fields (1503)

1. INTRODUCTION

Solar eruptions, especially those from active regions (ARs), are acknowledged to be the major driving sources of catastrophic space weather. The accompanying coronal mass ejections (CMEs) have become an important target for space weather monitored in remote observations and in in-situ measurements (Zhang et al. 2021). It

is generally believed that the physical essence of CMEs is the eruption of magnetic flux ropes (MFRs; Chen 1996; Titov & Démoulin 1999) that carrying plasma (Chen 2011). Therefore, studying the structure and evolution of MFRs is crucial to understand the physical mechanisms of CMEs and predict space weather. As it is currently difficult to measure the three-dimensional (3D) coronal magnetic field directly from observations, an alternative way of modeling coronal field with observed photospheric field used as boundary condition (Sakurai 1989; Solanki et al. 2006; Wiegmann et al. 2017; Wiegmann & Sakurai 2021; Zhu et al. 2022) or with the

rarely obtained chromospheric field (Wiegelmann et al. 2008; Harvey 2012; Jin et al. 2013; Lagg et al. 2017) has been implemented.

Overall, magnetohydrodynamics (MHD) approximation can provide a basic framework to outline the interaction between plasma and magnetic field in the solar atmosphere (Priest 2014). It is simplified under various conditions according to the two critical parameters of plasma β and Alfvén Mach number M_A (Gary 2001; Wiegelmann et al. 2017). Plasma β evaluates the dominance of the plasma gas pressure over the magnetic pressure, while the Alfvén Mach number estimates the flow speed over the Alfvén speed. Generally, MHD approximation should be adopted for the outer corona where the plasma flow and plasma gas pressure dominate. In regions with low M_A and finite β , e.g., in the upper photosphere and chromosphere, a steady-state derives the magnetohydrostatic (MHS) model with the Lorentz force being balanced by the plasma pressure gradient and gravitational forces (Wiegelmann et al. 2017). Under a further simplified condition of low M_A and low β , e.g., in the inner corona, the Lorentz force vanishes and the magnetic field becomes force-free, which is a state that assuming the dominance of the magnetic field over plasma. Models including nonlinear force-free field (NLFFF), linear force-free field (LFFF) and potential field are often applied to different force-free states (or current distributions) in terms of the force-free parameter (noted as α ; Wiegelmann 2008; Wiegelmann & Sakurai 2021). In particular, NLFFF extrapolations are favored for its relatively robust reconstructions and affordable computational resources in most cases. Various numerical methods have been developed to construct the NLFFF models, e.g., the optimization approach (Wheatland et al. 2000; Wiegelmann 2004), magneto-frictional method (Valori et al. 2007; Guo et al. 2016), MHD relaxation method (Jiang & Feng 2012), Grad-Rubin method (Grad & Rubin 1958; Amari et al. 2006; Gilchrist & Wheatland 2014) and flux rope insertion method (van Ballegoijen 2004; Su 2019).

Based on the force-free field methods, investigations have been carried out for understanding the initiation mechanism and the process of energy release during solar eruptions. Most of the works obtain an eruptive MFR with twist number around 1, and/or with decay index above the eruptive flux rope around $0.5 \sim 2$ (Sun et al. 2022) or $0.8 \sim 1.5$ (Zhong et al. 2021), which are consistent with the predictions of the kink instability and/or the torus instability. Nevertheless, the interplanetary magnetic clouds (MCs) originating from the sun however are found to have a wide range of twist number as high as 14.6 turns per astronomical unit from in-situ ob-

servations (Hu et al. 2014). Besides the possibility that the flux rope may evolve during its propagation in the interplanetary space (Wang et al. 2018), the discrepancy of the twist number obtained near the sun and in-situ may also lie in the force-free assumption that has been adopted for the entire atmosphere. By the MHD relaxation method, it is found that the non-force-free region can reach height of $1.4 \sim 1.8$ Mm above the photosphere (Zhu et al. 2016) and the non-force-freeness in the chromosphere has also been revealed in radiative MHD simulation (Leenaarts et al. 2015).

For attaining a reliable picture of the solar eruption, it is essential to study the magnetic configuration under non-force-free assumption that matches better with the physical situation, especially in the lower atmosphere. Therefore, an MHS extrapolation method (Zhu & Wiegelmann 2018) is developed for computing such magnetic configuration by taking into account the plasma pressure and gravity. It is found that, by applying both MHS and NLFFF extrapolation to a radiative MHD simulation (Cheung et al. 2019), the MHS method has more advantages in reconstructing long twisted magnetic field lines and in recovering the primary plasma structure in the lower atmosphere (Zhu & Wiegelmann 2019).

Comparison between observation and the extrapolation result is essential as the observation is the most important benchmark for validating any reconstruction method. For the NLFFF extrapolations, the associated QSLs could well define the main features during eruption, such as the initial position of flare ribbons and also the hot channels (Mandrini et al. 2006; Chandra et al. 2011; Zhao et al. 2016; Savcheva et al. 2016). For the MHS method, the field lines often reflect the chromospheric fine structures, such as the fibrils (Zhu et al. 2016, 2020) and brightenings (Zhao et al. 2017). It turns out that different methods have their advantages in different aspects and it is necessary to make an integration.

In this paper, we aim to show the performance of the MHS extrapolation in reconstructing 3D magnetic field of an active region. For this intention, AR 12158 which has been extensively studied (Cheng et al. 2015; Zhao et al. 2016; Zhou et al. 2016; Vemareddy et al. 2016; Duan et al. 2017; Lee & Magara 2018; Kilpua et al. 2021; Shen et al. 2022) is selected and we carry out the extrapolation with newly updated MHS method (Zhu & Wiegelmann 2022). The results are analyzed in details and are compared with the ones from other works. The paper is organized as follows: the observation characteristics are shown in Section 2.1 and the extrapolation method is introduced briefly in Section 2.2. The results

are displayed in Section 3 and we present the summary and discussions in Section 4.

2. OBSERVATIONS AND EXTRAPOLATION METHODS

2.1. Observations

NOAA AR 12158, which is selected for this case study, is observed near the disk center (N15E03 in heliographic coordinates) on 2014 September 10 by the Solar Dynamics Observatory (SDO; [Pesnell et al. 2012](#)). During its passage through the solar disk, an X1.6 class flare happens at 17:21 UT according to the soft X-ray 1–8 Å flux from the Geostationary Operational Environmental Satellites (GOES), and a halo coronal mass ejection (CME) event is subsequently accompanied (see CME catalog¹ ([Gopalswamy et al. 2009](#)) from Large Angle and Spectrometric Coronagraph (LASCO; [Brueckner et al. 1995](#)) aboard the Solar and Heliospheric Observatory (SOHO; [Domingo et al. 1995](#)). The observations from SDO at pre-eruptive phase are shown in Figure 1.

The magnetic field is observed by the Helioseismic and Magnetic Imager (HMI; [Schou et al. 2012](#)) and the product of Spaceweather HMI Active Region Patch (SHARP) series ([Bobra et al. 2014](#); [Hoeksema et al. 2014](#)) is usually employed for magnetic field extrapolation. For data labeled with 'hmi.sharp_cea_720s' as displayed in panel (a), it performs the projection and remapping of the observed vector magnetic field onto the heliographic Cylindrical Equal-Area (CEA) coordinate system ([Sun 2013](#)), and an equal pixel size (0.36 Mm) is derived in both longitude (or X) and latitude (or Y) direction.

Images of seven EUV channels from Atmospheric Imaging Assembly (AIA; [Lemen et al. 2012](#)) are shown in panels (b)–(h). An overall bright sigmoid structure is clearly seen in AIA 94 Å even at the pre-eruptive phase. Specifically, the overall sigmoid in AIA 94 Å shows separation in the middle, and the two separated parts which are pointed by arrows with J1 and J2 are the so-called double J-shaped structure. Filament fibrils, such as the ones pointed by arrows F1 and F2 in panel (g) are found in other wavelengths. The overall sigmoid structure has been reproduced with various extrapolations ([Zhao et al. 2016](#); [Kilpua et al. 2021](#)) while the fine structures, e.g., the dark fibrils, have no apparent correspondences in the previously obtained 3D magnetic field.

To better understand the detailed features mentioned in Figure 1, the EUV images at five selected time steps with a cadence of 1 hour are displayed in the top pan-

els of Figure 2 from left to right. The plus signs are added and annotated with 'A'–'E' for identifying the locations of different features. From 12:13 UT to 14:11 UT, the bright structure between B and C (pointed by the cyan arrows) evolves gradually. Such bright structure includes fibril-like features, which show overcrossing morphology at 12:13 UT and even twist at 13:19 UT. Apparent enhanced emission (pointed by white arrows) is found in AIA 94 and 131 Å at 14:11 UT. The above phenomenon and evolution characteristics may suggest the existence of magnetic flux rope with large twist, which is reproduced in our extrapolation that is introduced in Section 3.1, as well as the possible evidence of braiding and magnetic reconnection ([Awasthi et al. 2018](#)). The twist fibril-like feature is also identified in AIA 171 and 304 Å at 13:19 UT while the relevant emission enhancement at 14:11 UT is relatively weak. The sigmoid structure starts to brighten at 15:24 UT in AIA 94 Å, and a slender thread of brightening (pointed by yellow arrows) becomes visible in AIA 131, 171, 304 Å at 16:34 UT. These evolutionary processes also reveal the independence of J1 and J2 as separate parts and their relevance as a overall sigmoid. The observed sophisticated evolution before the eruption may imply the existence of complex magnetic structure in the active region, such as the braiding magnetic field lines ([Parker 1983](#); [Berger & Asgari-Targhi 2009](#); [Cirtain et al. 2013](#); [Pontin et al. 2017](#)) and the multi-flux-rope system ([Awasthi et al. 2018](#)). A detailed comparison with the magnetic field is shown in Section 3.1.

High resolution observations are also available for this event. The lower chromosphere is observed by the Big Bear Solar Observatory (BBSO)/Goode Solar Telescope (GST) in Near Infra-Red (NIR) channel, i.e., He I 10830 Å with a pixel size of 0.''079 ([Cao et al. 2012](#)). The slit-jaw images (SJI) in Ultra-Violet (UV) wavelengths, i.e., 2796 Å for the chromosphere and 1400 Å for the transition region, are observed by the Interface Region Imaging Spectrograph (IRIS, [De Pontieu et al. 2014](#)) with a pixel size of 0.''16. The observations with partial field of view (FOV) are displayed in Figure 3 for further comparison in Section 3.1.

2.2. MHS extrapolation method

The MHS model which solves the MHS equations by optimization method is developed by [Zhu & Wiegelmann \(2018\)](#) and optimized by [Zhu & Wiegelmann \(2019\)](#). To improve the computational efficiency, [Zhu & Wiegelmann \(2022\)](#) combines the MHS and NLFFF methods in which the MHS method is constrained in the very lower layer to produce magnetogram at a nearly force-free height for the NLFFF extrapolating upward.

¹ https://cdaw.gsfc.nasa.gov/CME_list/

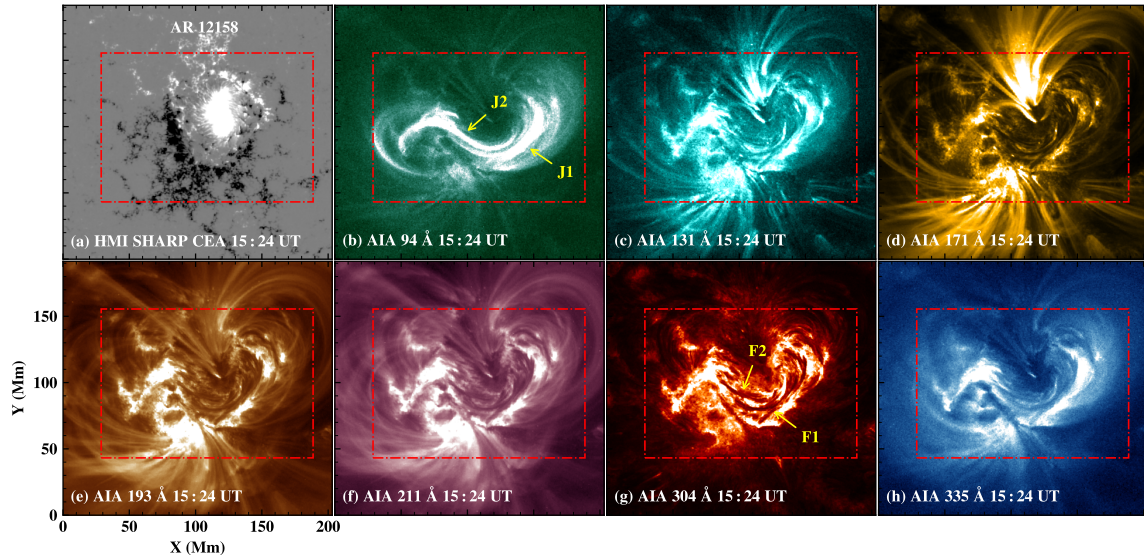


Figure 1. SDO observations of AR 12158 at 15:24 UT on 2014 September 10. Panel (a) shows the SHARP CEA remapped line-of-sight (LOS) magnetogram from SDO/HMI. Panels (b)–(h) show images of seven EUV channels from SDO/AIA. All the images are coaligned, and the red dashed boxes denote the major domain for the analyses in Section 3. An associated animation of panels (b)–(h) is available. The animation shows the evolution of various features such as sigmoid, hot channel, flare ribbon and the possible magnetic braiding during the period from 12:00 UT to 17:20 UT. The animation duration is about 64 s. (An animation related to this figure is available.)

The latest version of the model (Zhu & Wiegelmann 2022) is applied in the present work to obtain 3D magnetic field. The MHS equilibrium is described by the following equations:

$$\frac{1}{\mu_0}(\nabla \times \mathbf{B}) \times \mathbf{B} - \nabla p - \rho g \hat{z} = 0, \text{ satisfying } \nabla \cdot \mathbf{B} = 0. \quad (1)$$

where \mathbf{B} , p , ρ , are the vector magnetic field, plasma pressure and plasma density, while g and μ_0 denote the gravitational acceleration and vacuum permeability, respectively. More details can be found in Zhu & Wiegelmann (2022).

To reproduce the 3D magnetic field of AR 12158 with the MHS model, the vector magnetogram from SHARP CEA is adopted as the photospheric boundary as the MHS model is established in the Cartesian coordinate system. The radial component (B_r) of the photospheric magnetic field, which has original size of $564 \times 532 \text{ pixel}^2$, is shown in Figure 1(a). A volume of $444 \times 312 \times 200 \text{ pixel}^3$ with uniform pixel size of 0.36 Mm is extracted from the extrapolation result, and the bottom boundary is shown by the dashed box in Figure 1(a).

3. RESULTS

3.1. Magnetic field and the pre-eruption fine structures

The brightenings of the sigmoid structure before eruption have been identified in various observations (McKenzie & Canfield 2008; Zhang et al. 2012; Vemareddy & Zhang 2014; Cheng et al. 2014; Cheng &

Ding 2016) and also in the present work (see movie of Figure 1). They are suspected to be associated with magnetic reconnection, which is crucial for understanding the initiation and eruption of the flux rope system. The MHS model has an advantage in constructing the low-lying magnetic field lines, which enables a better comparison between the pre-phase reconnection and the magnetic field in the low atmosphere. The reconstructed magnetic field from MHS model is analyzed in detail to show its correspondence firstly with the brightenings in AIA observations which covers a range from chromosphere to the corona, and then specifically with the dark/bright fibrils in the extremely high-resolution observations at different layers of chromosphere and the transition region.

The field lines from MHS model are displayed in the bottom panels (e)–(g) of Figure 2, with color-coded field-lines' groups overlaying on different features observed in AIA 131Å, 304Å, 94Å from left to right. In general, there are two main flux ropes represented by the field lines in yellow (MFR1) and green (MFR2) respectively. The surrounding field lines intimately related to MFR1 are coded with cyan and orange, while the left loop system is shown in purple.

The field lines in cyan, which are beneath MFR1 for the left part and over-wrapping the latter at the right end, correspond to the dark region between C and D in AIA 304 Å (see panel (f)). The combination of MFR1 and field lines in cyan may represent the emission en-

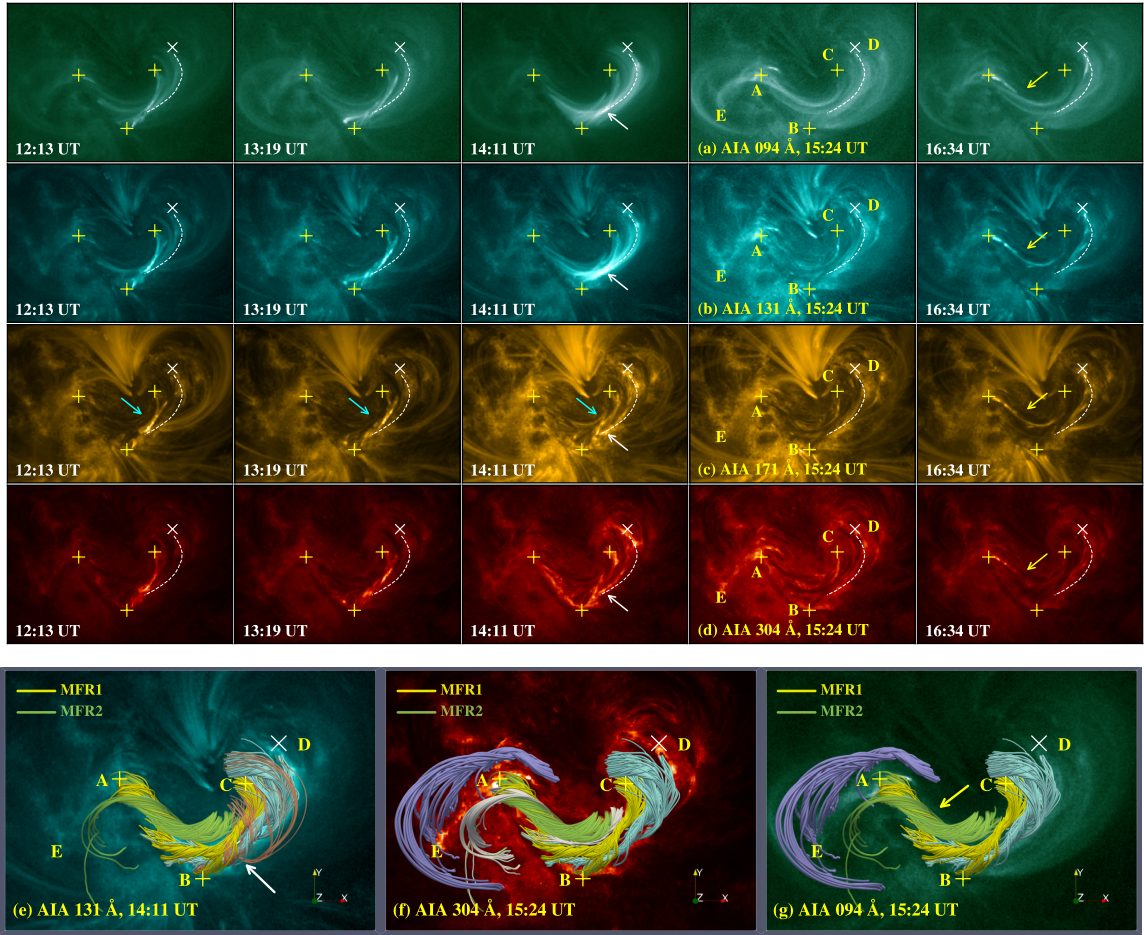


Figure 2. SDO observations at multiple time steps and the reconstructed magnetic field. Top panels: time evolution of the event in EUV images from SDO/AIA 94, 131, 171, and 304 Å at five time steps (with 1 hour cadence) before the X-class flare. Bottom panels: the reconstructed magnetic field lines from MHS extrapolation at 15:24 UT are overlaid on the AIA images at 14:11 UT for 131 Å, 15:24 UT for 304 and 94 Å for comparison. Different colors show the magnetic field lines with different connectivity. All the plus signs and dash lines in the panels are labeled for the reference of the locations for different structures.

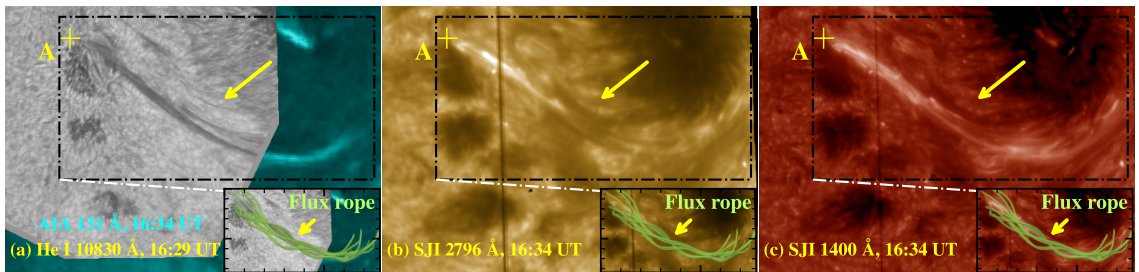


Figure 3. High-resolution observations with partial field of view (FOV) as an extension of Figure 2. Panel (a): the grayscale image is He I 10830 Å taken by BBSO/GST at 16:29 UT, and its missing FOV is filled with AIA 131 Å at 16:34 UT as the background. Panels (b)–(c) are observations from SJI 2796 and 1400 Å at 16:34 UT. The box at the lower-right corner of each panel shows the top view of magnetic flux rope overlaid on the corresponding sub-region.

hancement of AIA 94, 131Å at 14:11 UT. The region indicated by the white arrow in panel (e), which has overlapping field lines in orange on top of the MFR1 and

field lines in cyan, may be responsible for the braiding features before 14:11 UT. In addition, the right branch of MFR1 between B and C seems to be consistent with

the other dark stripe that is next to the aforementioned predominant one between C and D in AIA 304 Å. The field lines in purple have their feet anchored near the bright belt between A and E of AIA 304 Å, while the loops themselves tend to coincide with the outer loops of AIA 94 Å as shown in panel (g).

The primary part of MFR2 (field lines in green) is cospatial with the slender emission between A and B at 16:34 UT, and the left extension tends to outline the loop between A and E of AIA 94 Å. In particular, in the high-resolution images of He I 10830 Å, SJI 2796 and 1400 Å as shown in Figure 3, the slender dark/bright fibrils are in good agreement with the position of the magnetic flux rope MFR2 as shown in the lower-right corners. In Figure 3(a), the He I 10830 Å image has a smaller FOV, and its missing part is filled with AIA 131 Å. We notice that the cold component of the slender feature in 10830 Å is well connected to the hot component in 131 Å, indicating the multi-temperature components for such structure.

The above comparison between magnetic field lines of MHS extrapolation and observations from multiple layers, ranging from chromosphere consecutively to the corona, reveals good correspondence, which is rarely achieved.

3.2. EUV Eruptive Features and QSLs

To show the ability of the MHS modeling in inferring the eruptive features, such as flare ribbons and hot channels, the squashing factor Q are calculated and the results are displayed in Figure 4.

The Q factor measures the gradients of magnetic connectivity in a volume, and the region with large Q value is defined as quasi-separatrix layer (QSL, Démoulin et al. 1996; Titov et al. 2002), which separates the region of distinct flux systems. Hence, Q map is a good indicator for ascertaining the characteristic structure of magnetic field. The method for calculating the Q factor can be found in Zhao et al. (2014) and can also refer to a FORTRAN parallel routine from Liu et al. (2016)².

The flare ribbons in AIA 304 Å are displayed in Figure 4(a) and the sigmoidal hot channel in AIA 94 Å is shown in Figure 4(b). The calculated Q map at the lower layer is displayed in Figure 4(c), while the one along the vertical dot-dashed line in Figure 4(c) is shown in Figure 4(d). The contours of Q are overlaid on AIA 304 and 94 Å, respectively. An S-shaped QSL is identified in Figure 4(c). The S-shaped QSLs generally coincide with the

hot channel (L1) in AIA 94 Å and its hook parts roughly match the brightenings of the flare ribbons (R1 and R2) in AIA 304 Å. Such correspondence has also been derived in Zhao et al. (2016) with a NLFFF-based method called Current-Field Iteration in Spherical Coordinates (CFITS; Gilchrist & Wheatland 2014).

In the vertical slice in Figure 4(d), three white dashed lines are displayed to provide reference for the boundaries of the flux ropes. As the QSLs obtained in the present work have many fine structures, different from the ones obtained by force-free extrapolation (such as in Zhao et al. 2014, 2016), the flux rope boundaries are selected manually according to the rough locations with large Q values. The inner circle-shaped QSLs, which indicate a strongly twisted core part of MFR1, is wrapped by the outer QSLs. The height of MFR1 is about 8 Mm, which is lower than the MFR derived by CFITS (~ 25 Mm). A second main flux rope (MFR2) is located adjacent to MFR1 and the main body is also outlined with the dashed line. The boundary of MFR2 is not as apparent as MFR1 in the Q map, which is possibly due to the slice location that is not placed at the well-twisted region of field lines. Moreover, there are high Q regions at the bottom below 5 Mm, yet the existence of hyperbolic flux tube (HFT), which indicates the most probable reconnection site among the high Q regions, cannot be distinguished effectively. It implies that the possible reconnection may distribute in a diffuse region, different from the results of CFITS which obtains a clear HFT beneath the magnetic flux rope.

3.3. Magnetic-field Configuration and QSLs

Magnetic configuration and related QSLs are explicitly revealed in Figure 5 from 3D perspective. As the QSLs at the vertical slice have tremendous fine structures, we have used a vertical black-white sketch, as shown in the upper right corner of panel (b), as a proxy to better display the correspondence. The sketch is obtained by extracting the main structures associated with the magnetic flux ropes as we have annotated with dashed lines in Figure 4(d). The outer part of MFR1 is displayed with black while the inner part inside is shown with white. As no fine structures are identified to be associated with MFR2, the whole flux rope region is shown with black. The annotations in the sketch are exactly the same as in Figure 4(d). The colors of the field lines in Figures 5(a)–(c) are coded with the twist number that is calculated through one common axis, i.e., MFR1 axis. More details of the twist number calculation is described in Section 3.4.

The displayed field lines reveal a complex connectivity. The magnetic field lines in the lower altitude (the

² <http://staff.ustc.edu.cn/~rliu/qfactor.html> or an updated site <https://github.com/el2718/FastQSL> according to Zhang et al. (2022)

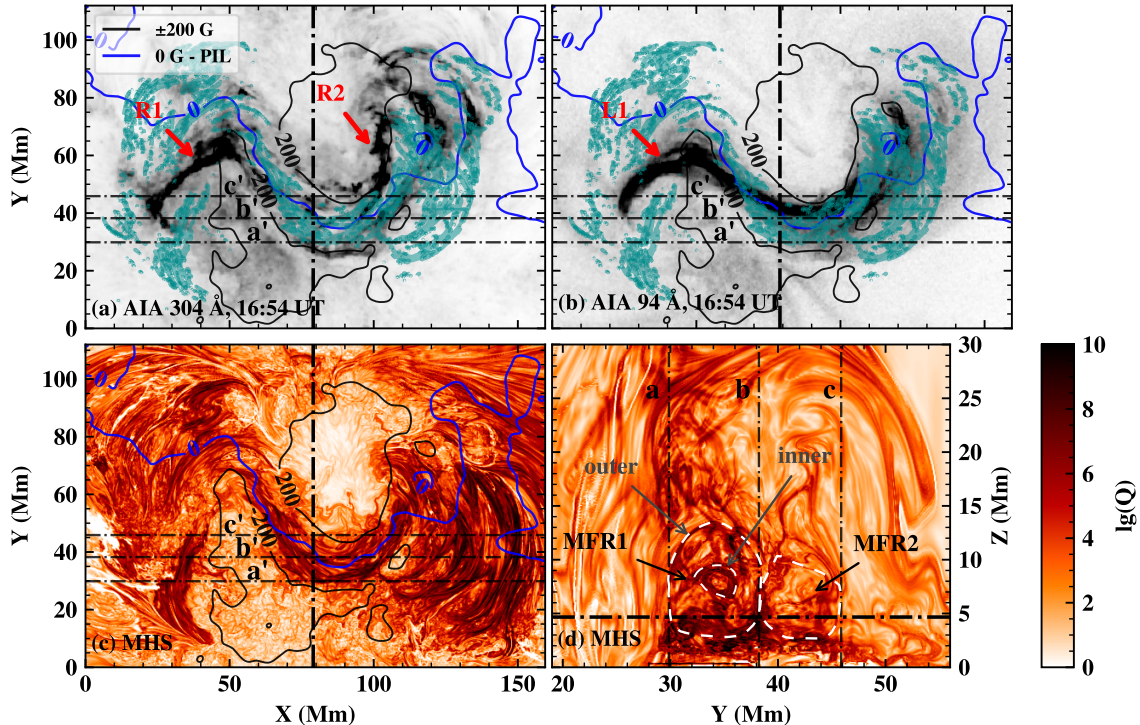


Figure 4. Comparison between the eruptive features and the calculated squashing factor Q of the magnetic field. The AIA 304 and 94 Å images with reversed grayscale are shown in panels (a) and (b), respectively. Brightenings are displayed in dark color. The 2D distributions of Q are displayed in panels (c) and (d). The contours of QSLs from panel (c) with $\lg(Q) = 6.5$ are overlaid on panels (a) and (b) in green, by extracting the relevant parts corresponding to the brightening regions in AIA 304 Å. The blue and dark contours in panels (a)–(c) show the B_z component from the potential field, with levels of 0 and ± 200 G. The vertical dot-dashed lines in panels (a), (b) and (c) denote the slice position of panel (d) while the horizontal dot-dashed line in panel (d) shows the layer where the Q values are sampled and displayed in panel (c). Three vertical planes are used to identify the location of the flux ropes, which have intersections on the lines a, b, c on the vertical cut shown in panel (d), and a', b', c' on the horizontal cut in panel (c). The white dashed lines in panel (d) are manually selected to mark the boundary of the flux ropes.

aforementioned diffuse regions of possible reconnection from the distribution of QSLs) are displayed in Figure 5(b) individually. They are roughly along the PIL, and they show the braiding characteristics and a coupling with the axis of MFR1 to a certain extent. The core field lines of the MFR1 and MFR2 are displayed separately in Figure 5(d), according to the QSLs as shown in the black-white sketch. A slightly smaller twist is confirmed for MFR2, which is located in the north of the highly twisted MFR1.

The above results again explicitly show that, unlike the standard single-core MFR picture appearing in other cases (Zhao et al. 2016; Kilpua et al. 2021; Jiang et al. 2021), the sigmoidal configuration obtained in MHS extrapolation primarily consists of two independent but slightly coupled MFRs. The latter one, together with the ambient field lines, corresponds well to the double J-shaped hot channel in AIA 94 Å as shown in Figure 2(g).

3.4. MHD instabilities

The helical kink instability (KI; Török et al. 2004) and torus instability (TI; Kliem & Török 2006), as two basic mechanisms of ideal MHD instability, are usually invoked to be responsible for triggering and driving the MFR eruption, and are characterized by the parameters of twist number and decay index, respectively.

3.4.1. Twist Number

The KI suggests that the instability is triggered when the twist (Berger & Prior 2006) of the MFR exceeds a critical value T_c (well-known as ~ 1.25 turns in a force-free MFR suggested by Hood & Priest 1981). Based on Berger & Prior (2006), there are two typical definitions for the twist number. One measures the number of turns between two infinitesimally close magnetic field lines winding about each other and a fast code is developed by Liu et al. (2016) to calculate the twist in a volume. The other defines the twist number as the field lines wind about a common axis. The twist density of a

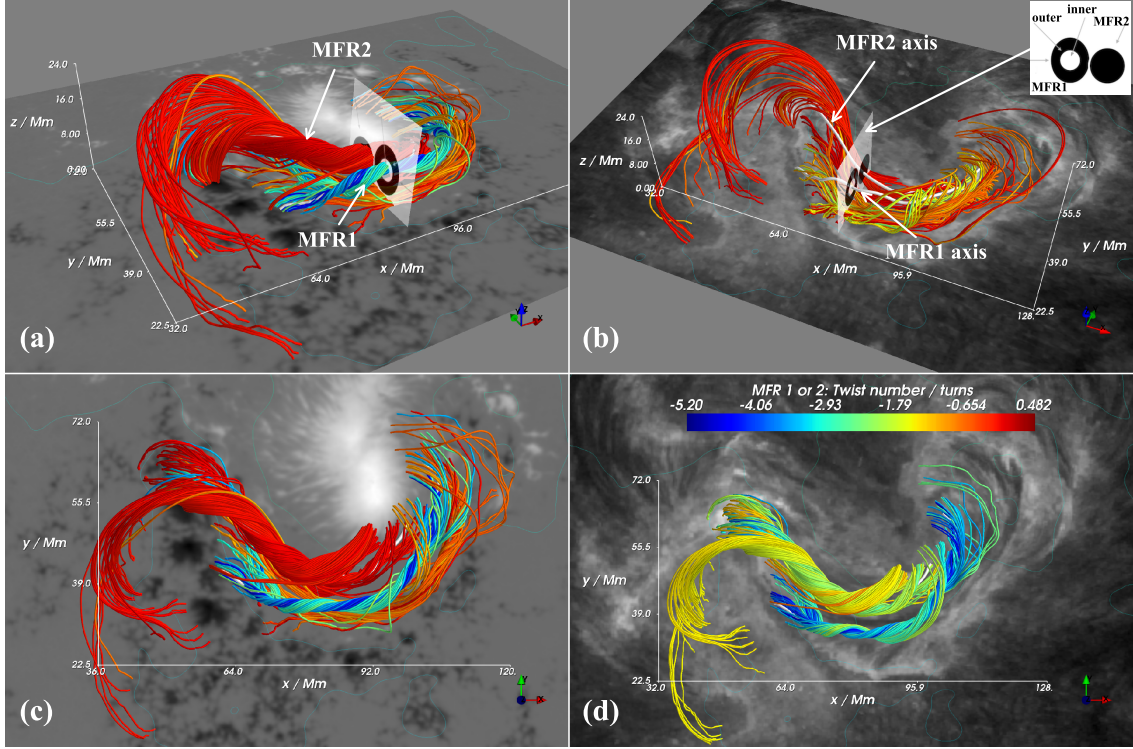


Figure 5. Magnetic connectivity and twist number of the flux rope system are displayed. All field lines are colored with the twist number and the colorbar is shown in panel (d). One common axis (MFR1 axis) is selected for calculating the twist number in panels (a)–(c), while two separate axes, i.e., MFR1 axis and MFR2 axis, are adopted in panel (d) for calculating the twist number of MFR1 and MFR2, respectively. The 2D vertical slice with black-white sketch as shown in the corner of panel (b) is inserted in panels (a) and (b) with a view angle of 3D for emphasizing the connectivity.

curve $\mathbf{y}(s)$ around the smooth common axis curve $\mathbf{x}(s)$ is defined as

$$\frac{d\Phi}{ds} = \frac{1}{2\pi} \mathbf{T}(s) \cdot \mathbf{V}(s) \times \frac{d\mathbf{V}(s)}{ds}, \quad (2)$$

where s measures arc length from an arbitrary starting point on $\mathbf{x}(s)$, while $\mathbf{T}(s)$ is the unit tangent vector to $\mathbf{x}(s)$, and $\mathbf{V}(s)$ is the unit vector normal to $\mathbf{T}(s)$ pointing from $\mathbf{x}(s)$ to $\mathbf{y}(s)$. The final twist number T is obtained by integrating Equation (2) along the axis $\mathbf{x}(s)$.

The application of the latter method is to find a common axis among the magnetic field lines at the first step, and then to calculate the twist number of each curve around the axis. The axis and computational region are determined naturally by QSLs as they could depict the main body of an MFR (Guo et al. 2013, 2017b, 2021).

To better interpret the physical meaning, we adopt the latter definition to calculate the twist number with the code from Guo et al. (2010, 2013)³. One common axis, i.e., the axis of MFR1, has been tested for calculating the

overall twist number and the results are shown in Figures 5(a)–5(c). As the main body of MFR2 departs from the axis of MFR1, the twist number of MFR2 is small in this manner. A separate axis is therefore selected for MFR2 and the twist number is calculated individually for MFR1 and MFR2, as demonstrated in Figure 5(d).

The highest twist number can reach 3 turns for MFR2 and 5 turns for MFR1, and the average values are about 1.6 and 3 turns, respectively. The results show that, in this case, the MHS equilibrium has larger twist numbers than T_c for triggering eruption. The quantitative results of twist number in the present work and other investigations are also listed in Table 1. As there are inner part and outer part for MFR1 as displayed in Figure 5b, the twist number is calculated referring to the same axis but for two conditions, with one for the inner part only and the other one for the overall of the flux rope including the inner part and outer part. As MFR2 has less complex distribution of the magnetic field lines, twist number has been calculated referring to MFR2 axis for the overall flux rope.

³ https://github.com/njuguoyang/magnetic_modeling_codes

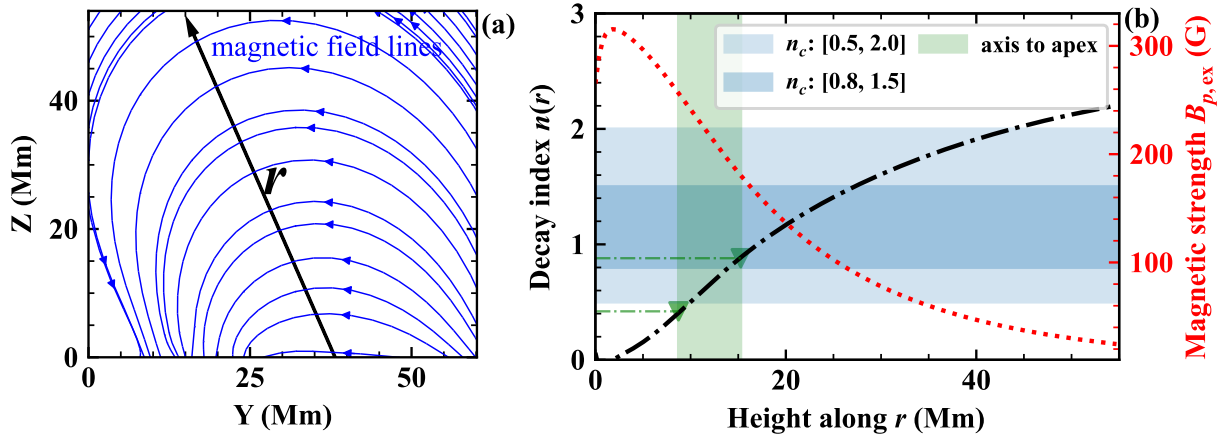


Figure 6. Decay index. Panel (a) displays the vertical slice like those in Figure 4(d) but with field lines which tracing the projected component of the potential field in the Y-Z plane, and the oblique line with arrow depicts the direction r for calculating the decay index. Panel (b) shows the profiles of the decay index $n(r)$ (black dot-dashed line) and of the strength of external poloidal magnetic field $B_{p,ex}$ (red dotted line). The blue and light blue shaded areas denote the reference range of critical decay index n_c from Zhong et al. (2021) and Sun et al. (2022), respectively. The green shaded area shows the height ranges from the MFR core to the apex along the direction of r . The lower and upper limits of decay index are marked by ∇ .

The TI is suggested to have a significant effect on the eruption of an MFR due to the strapping force of the background field. Recently, a more relevant field ($B_{p,ex}$; Duan et al. 2019; Zhong et al. 2021), which is the component of the potential field that is perpendicular to both the axis and the erupting path of the MFR, is adopted for calculating the decay index. Like in other works (Bateman 1978; Jiang et al. 2014), the decay index of $B_{p,ex}$ is written as

$$n(r) = -\frac{d \log(B_{p,ex})}{d \log(r)}, \text{ or } n(r) = -\frac{r}{B_{p,ex}} \frac{dB_{p,ex}}{dr}. \quad (3)$$

The obtained decay indices of the MHS equilibrium are shown in Figure 6. The black arrow r in panel (a) indicates the path to calculate decay index, which roughly follows the direction of the ridge of the magnetic field lines. We find that it has the decay index of about $0.4 \sim 0.9$, as shown in Figure 6(b). Critical range of the decay index has been found within $0.8 \sim 1.5$ in Zhong et al. (2021) and within $0.5 \sim 2.0$ in Sun et al. (2022). According to such criteria, the MHS model in the present work is able to trigger torus instability. Nevertheless, the relative small index of MHS might be related with the low-lying flux rope, where the strapping field above could still be relatively strong.

3.5. Magnetic Energy and Helicity

Magnetic free energy and magnetic helicity, which are frequently investigated in previous studies, are also explored in the present work. Magnetic free energy is believed to be the upper limit of the energy release, while

magnetic helicity essentially manifests the complexity of the magnetic field (Berger & Field 1984).

3.5.1. Magnetic Energy

The energy stored in magnetic field that can power eruptions is the free energy, which is estimated as:

$$E_{\text{free}} = \int_V \frac{B^2}{8\pi} dV - \int_V \frac{P^2}{8\pi} dV = \int_V \frac{B^2 - P^2}{8\pi} dV, \quad (4)$$

where B and P are the strength of non-potential field and reference potential field respectively. The latter one is obtained based on the Green's function method (Chiu & Hilton 1977; Sakurai 1982; Wiegmann et al. 2005), in order for the comparison of free energy in Section 3.5.3. The integrand denotes the energy density distributed over the computational domain V . By integrating energy density along Z direction and multiplied by the surface element $dS = dx dy$ (Jiang et al. 2014), a 2D distribution of free energy $E_{\text{free}}(x, y)$ is obtained as shown in Figure 7(a). The result indicates that the free energy of MHS has high values distributed along MFR1 and MFR2 (also see Figure 7 (b-c) for 3D renderings). It is worth noting that the MHS model has conspicuous free energy in the region that is outlined with a white box in Figure 7(a), where Cheng et al. (2015) investigated the shearing flow and magnetic cancellation at the same region. We also notice the high values in the sunspot region. As discussed by Borrero & Ichimoto (2011) and Tiwari (2012), sunspots tend to be non-potential which implies that the existence of free energy, and the consideration of plasma effect in MHS model may also lead to free energy.

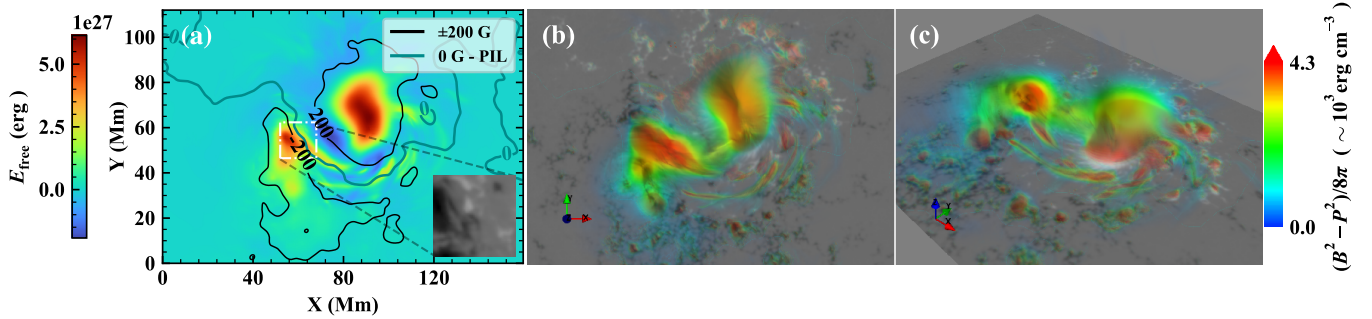


Figure 7. Distributions of free energy in 2D and 3D. The 2D map in panel (a) displays the integrals along Z direction with several layers covering the primary structure. The contours in cyan and dark show the B_z component from the potential field with levels of 0 and ± 200 G as in Figure 4. The white dot-dashed box denotes the site of shearing flow and magnetic field cancellation suggested by Cheng et al. (2015). The 3D maps in the right two panels show the volume rendering of $(B^2 - P^2)/8\pi$ with bird view and side view, respectively.

3.5.2. Magnetic Helicity

Magnetic helicity, in its original definition, is the volume integral of the scalar product between vector potential and vector magnetic field. It measures the linkage of a bundle of magnetic field lines, and is related to the topological concepts such as Gauss linking number, and the usually used twist number and writhing number (Berger & Field 1984; Moffatt & Ricca 1992; Berger & Prior 2006). For solar active region, relative magnetic helicity as a conserved quantity is given by Berger & Field (1984) and Finn & Antonsen (1985) for the domain of volume V :

$$H_m = \int_V (\mathbf{A} + \mathbf{A}_p) \cdot (\mathbf{B} - \mathbf{P}) dV, \quad (5)$$

where \mathbf{A} and \mathbf{A}_p are the vector potentials of \mathbf{B} and \mathbf{P} . Potential field \mathbf{P} is usually adopted as the reference field. The boundary condition $(\hat{\mathbf{n}} \cdot \mathbf{B})|_{\partial V} = (\hat{\mathbf{n}} \cdot \mathbf{P})|_{\partial V}$ is adopted here to keep H_m gauge-invariant. This form of helicity calculation used within a considered volume is also known as the finite volume method, which enables a direct comparison of H_m computed from different magnetic fields (Valori et al. 2012). More methods of helicity estimation have been proposed, such as twist-number (TN), helicity-flux integration (FI), connectivity-based (CB), see Valori et al. (2016), Guo et al. (2017a) and Thalmann et al. (2021) for an overview.

As shown in previous works (Berger 1999, 2003; Guo et al. 2017b), the helicity in a finite volume can be decomposed into two components, with one component representing the contribution from the magnetic field that carries local currents and the other component standing for the contribution from the potential field and magnetic field generated by local currents. The former component is called current-carrying helicity as H_J

in the present work and is calculated as follows:

$$H_J = \int_V (\mathbf{A} - \mathbf{A}_p) \cdot (\mathbf{B} - \mathbf{P}) dV. \quad (6)$$

Solar eruptions often show highly twisted magnetic flux rope, which initiated a twist number method for the helicity calculation (Guo et al. 2010, 2013, 2017b). By neglecting the contribution from writhe, and also the one from the mutual helicity between magnetic flux rope and ambient field, the twist helicity is calculated as follows:

$$H_{\text{twist}} \approx T\Phi^2, \quad (7)$$

where $\Phi = \iint B_x dydz$ is the axial magnetic flux.

The relative helicity, current-carrying helicity and twist helicity are then obtained and are shown in Table 1. It is found that $|H_{\text{twist}}|$ of the MHS model is smaller than $|H_J|$, which is probably due to the fact that the local current is not completely limited to the volume occupied by the MFR. In addition, the MHS model has two coupled MFRs and braiding with the surrounding magnetic field, thus the mutual helicity is underestimated in the computation.

The role of magnetic helicity for indicating the solar eruptions has been extensively discussed (Toriumi & Park 2022). MHD simulations (e.g., Pariat et al. 2017; Zuccarello et al. 2018; Linan et al. 2018) suggest that helicity ratio, i.e., $|H_J|/|H_m|$ is a promising proxy of solar eruptivity. In observations, statistics (Gupta et al. 2021) and case studies (James et al. 2018; Moraitis et al. 2019b; Thalmann et al. 2019) using force-free modeling also show that $|H_J|/|H_m|$ has advantages in predicting the eruptive potential of a flaring AR. It is mainly characterized by the higher $|H_J|/|H_m|$ values (e.g., >0.1 in Gupta et al. 2021) for CME-productive active regions, and the reduction of $|H_J|/|H_m|$ during eruptions. In the present work, the helicity ratio given by MHS is about

0.06. By inspecting the MHS data, we find that there are some positive values in the volume of integrand from equation (6), although the integral helicity of the entire computational volume is negative. The absolute ratio of the positive integral to the negative one of H_J is about 0.5, which naturally leads to a small value of current-carrying helicity integration as the two components are not treated separately. Such difference is inherently dependent on the model that is adopted for reconstructing the magnetic configuration. Nevertheless, there are exceptions of the statistical threshold (Thalmann et al. 2021; Gupta et al. 2021) and whether there is a universal criterion for extrapolations with different assumptions, e.g., the force-free and non-force-free ones, requires further examinations with more samples (Moraitis et al. 2019b; Toriumi & Park 2022).

3.5.3. Comparison with previous results

AR 12158 has been extensively studied in various aspects and with various extrapolation methods, here we present some comparisons between our results and others in Table 1. Duan et al. (2017) compared different extrapolations with NLFFF code (CESE-MHD-NLFFF, by Jiang & Feng 2013) and non-force-free field code (NFFF, by Hu & Dasgupta 2008; Hu et al. 2010). Comparing to NLFFF2 and NFFF, MHS obtains free energy and relative helicity in the same order of magnitude. In the aspect of magnetic configuration, MHS obtains two twisted flux ropes while the other methods obtained sheared arcades or one coherent flux rope with medium twist number. The above results demonstrate that, although the plasma forces bend the magnetic field lines to form a non-force-free configuration in MHS method, the non-force-freeness does not necessarily bring in more energy or helicity.

4. SUMMARY AND DISCUSSION

4.1. Summary

Magnetic field in the solar atmosphere, which is responsible for solar eruptions, interacts with plasma in nature, especially at the lower atmosphere such as the photosphere and lower chromosphere where plasma β is non-negligible. To construct a 3D magnetic field above the photosphere, which could imitate the observations in more details, it is necessary to consider the contribution of plasma effect. In this paper, we reconstruct the magnetic field of AR 12158 by using the MHS extrapolation method, evaluate its performance in reproducing the observations in multiple wavelengths ranging from chromosphere to the corona. We also discuss the magnetic topology and connectivity, decay index and twist number, and the magnetic energy and relative helicity.

The EUV observations before eruption imply that AR 12158 contains abundant atmospheric structures, such as the S-shaped structure composed of two separated J-shaped segments in AIA 94 Å, the dark stripes in AIA 304 Å, and the twisted braiding structure in multi-wavelengths. The high resolution observations in IR and UV also show the multi-temperature fibrils. All the above mentioned fine structures, especially the braiding structures, are in good agreement with the reconstruction results of the MHS model. The braiding required by Parker-type nanoflare scenarios prefers such a non-force-free environment (Aschwanden 2019) like in the chromosphere and transition region, and it could be difficult to reproduce from the methods with force-free assumption. During the eruption, magnetic topology from the MHS model is co-spatial with the flare ribbons as well as the hot channel, like the one obtained by the NLFFF extrapolation (Zhao et al. 2016).

The MHS model distinguishes two separate but weakly coupled flux rope systems (MFR1 and MFR2). MFR1 has an average twist of about 3 turns and a maximum one of about 5 turns for the core part, while MFR2 has a twist number of about 1 ~ 2 turns which is close to the result in Zhao et al. (2016) and Kilpua et al. (2021). For the overall asset, such as the total amount of free energy and relative helicity, the MHS method as well as other NLFFF and NFFF methods, derive values on the same order of magnitude, i.e., $\sim 10^{32}$ erg and $\sim 10^{43}$ Mx² respectively.

This work shows that although the estimated total amount of energy and helicity are on the same order for different extrapolation methods, there are differences in the specific magnetic configuration, thus leading to different understanding of the eruption. The force-free field models compared in this work enable a general description of the active region magnetic field. Detailed magnetic structures, which are crucial for understanding the evolution of flux rope as well as the trigger of eruption at the initial phase, have been acquired from the MHS model with consideration of the plasma. Beyond the case study, comparisons need to carry out with more samples and also with other extrapolation methods in future to validate the advantage of the non-force-free method in a more general sense.

4.2. Further Discussion

High twist number is obtained from the MHS method while only sheared arcades or weakly twisted flux rope have been reproduced from other NLFFF methods. The validation of such high twist and the associated MHD instability are further discussed in this subsection.

4.2.1. High Twist Number

Table 1. Magnetic quantities derived from different methods

Model	E_{tot} (10^{32} erg)	E_{pot} (10^{32} erg)	E_{free} (10^{32} erg)	$E_{\text{free}}/E_{\text{pot}}$	H_{in} (10^{43}Mx^2)	H_{J} (10^{43}Mx^2)	H_{twist} (10^{43}Mx^2)	$ \overline{T_{\text{w}}} $ (Turn)
MHS	11.15	9.90	1.25	12.7%	-1.60	-0.09	-0.007 ± 0.004	MFR1, 1.39 ± 0.92^a , 3.06 ± 0.82^b MFR2, 1.59 ± 0.40^a ,
NLFFF1	11.5	11.7	-0.18	-1.5%	-1.60	-	-	≤ 1.0
NLFFF2	11.1	10.0	1.10	10.9%	-2.03	-	-	≤ 1.0
NFFF	14.8	11.8	3.02	25.6%	-2.36	-	-	≤ 1.0
CFITS	-	-	-	-	-	-	-	$1 \sim 2$

NOTE—NLFFF1, NLFFF2, and NFFF are results from [Duan et al. \(2017\)](#), and their twist number are computed by the first definition. The NLFFF1 and NLFFF2 use unprocessed and preprocessed vector magnetograms as boundaries, respectively. The negative free energy in NLFFF1 arises probably due to inconsistency between the unprocessed magnetogram and the force-free approximation. CFITS represents the result from [Zhao et al. \(2016\)](#) with an approximate twist number.

^a Twist number for the overall flux rope.

^b Twist number for the inner core part of MFR1.

By applying an analytical MHS solution ([Low 1991](#)) to a magnetogram with two current systems (one following along and the other across the magnetic field), [Low \(1992\)](#) found that the magnetic field lines become more complex with elongated and multi-helical features due to the cross-field current associated with plasma effect. Although the features are observed in the analytical model, they provide some instructive glimpse of highly-twisted magnetic flux interacted with plasma in real atmosphere.

In the aspect of observations, the rotation of sunspot may contribute to the high twist of magnetic field lines. Such contributions have been identified in [Vemareddy et al. \(2016\)](#) and [Brown & Walker \(2021\)](#) for AR 12158, and in AR 11943/11944 ([Duan et al. 2021](#)) for the flux rope structure. Twist number as high as 6 turns has been obtained in the latter case. Interplanetary magnetic cloud with high twist number is frequently observed at L1 point ([Wang et al. 2016](#)), indicating the eruptive counterpart near the sun may be highly twisted originally.

4.2.2. MHD instability

MFR with large twist number is considered to be explosive due to kink instability. Both the theories and observations demonstrate that the critical twist number has a large range and is influenced by such as the external magnetic field, the plasma flow, and plasma β (see discussion in [Guo et al. 2021](#)).

The maximum twist number ($|T|_{\text{max}}$) was found to be sensitive during flares ([Liu et al. 2016](#)). Such parameter was employed by [Duan et al. \(2019\)](#) as a controlling

parameter for investigating the kink instability of the pre-flare MFRs in a statistical manner. Their results, which are based on the force-free assumption, demonstrate that flare events with $|T|_{\text{max}}$ exceeding its critical value ($|T|_{\text{c}}$) have a high possibility to erupt successfully. Lower limit and average values of $|T|_{\text{c}}$ from statistics are suggested to be 2 and 2.83 ± 1.31 turns respectively.

Meanwhile, previous works ([Dungey & Loughhead 1954](#); [Hood & Priest 1979](#); [Bennett et al. 1999](#); [Baty 2001](#)) estimated the critical value, $T_{\text{c}} = \frac{\omega_{\text{c}}L}{2\pi a}$, of a uniform twisted MFR with axial length L and minor radius a , suggesting a higher value for thinner MFR. Considering the non-force-free state in the present work, the parameter ω_{c} , which depends on detailed configuration of an MFR, is selected to be around 2 ([Dungey & Loughhead 1954](#); [Bennett et al. 1999](#); [Wang et al. 2016](#)). With the aspect ratio L/a being estimated as 18 for MFR1, we derive a critical twist of about 5.7 turns which is greater than the $|T|_{\text{max}} \approx 5$ turns of MFR1. Under this estimation, the stability of MFR1 is consistent with the half eruption that discussed in [Shen et al. \(2022\)](#) where they show the erupting of the left J-shaped sigmoid that corresponds to MFR2 in the present work.

Acknowledgements. We thank Dr. Yingna Su for an internal review of this paper. We also thank the open-source tools ([Mayavi](#) and [ParaView](#)) for 3D scientific data visualization. Data from observations are provided by NASA/SDO and the HMI and AIA science teams, by the IRIS and BBSO science teams. IRIS is a NASA small explorer mission developed and oper-

ated by LMSAL with mission operations executed at NASA ARC and major contributions to downlink communications funded by ESA and the Norwegian Space Center. BBSO operation is supported by NJIT and US NSF AGS-1821294 grant. GST operation is partly supported by the Korea Astronomy and Space Science Institute, the Seoul National University, and the Key Laboratory of Solar Activities of Chinese Academy of Sciences (CAS) and the Operation, Maintenance and Upgrading Fund of CAS for Astronomical Telescopes and Facility Instruments. F.Y., J.Z., and Y.S. acknowledge the support by 2022YFF0503001 and National Natural Science Foundation of China (grant Nos. 11820101002). J.Z. acknowledges the supports by National Natural Science Foundation of China, Grant No. 12233012, 11503089, U1731241 and Chinese Academy of Science

Strategic Pioneer Program on Space Science, Grant No. XDA15052200, XDA15320103, XDA15320301, and mobility program (M-0068) of the Sino-German Science Center. X.Z. acknowledges financial support by National Key R&D Program of China (2021YFA1600503), mobility program (M-0068) of the Sino-German Science Center, and NSFC grant 11790301. Y.G. was supported by NSFC (11773016, 11961131002, and 11533005) and 2020YFC2201201. This work is supported by Open Research Program No. KLSA202112 of CAS Key Laboratory of Solar Activity. This research is supported by the International Space Science Institute (ISSI) in Bern and the ISSI-BJ in Beijing, through ISSI International Team project 568 and ISSI-BJ International Team project 55 (Magnetohydrostatic Modeling of the Solar Atmosphere with New Datasets).

APPENDIX

A. SUPPLEMENT ON MAGNETIC HELICITY

The potential field solved with either one bottom boundary or six boundaries can be conveniently used for the calculation of relative magnetic helicity under the original DeVore's method (DeVore 2000; DeVore & Antiochos 2000) or the DeVore-gauge based finite volume (FV) method (e.g., using DeVore_GV gauge in Valori et al. 2012), respectively. For the latter one, there are many ways to solve the 3D Laplace problem numerically as the first step, such as the Helmholtz solver in the Intel[®] Mathematical Kernel Library (MKL), the HW3CRT routine in the FISHPACK library (Swarztrauber & Sweet 1979), or the fast Fourier transform (FFT) based method as described in Valori et al. (2016).

It should be noted that the DeVore's method is defined in semi-infinite space ($z \geq 0$). In practice, the volume integrals is inevitably limited to a finite volume, so the choice of integral volume destroys the original gauge invariance. The FV method is defined in a finite volume, which provides a way to make the helicity values from different magnetic fields comparable. Therefore, the FV method is recommended and widely used in the comparative or statistical study related to relative magnetic helicity (e.g., Gupta et al. 2021) in recent years, and is also adopted in this work.

According to the FV method from Valori et al. (2012), we compute \mathbf{A} and \mathbf{A}_p under DeVore_GV gauge in a volume $V = [x_1, x_2] \times [y_1, y_2] \times [z_1, z_2]$ as follows:

$$\mathbf{A} = \mathbf{b} + \hat{\mathbf{z}} \times \int_z^{z_2} \mathbf{B} dz', \quad (\text{A1})$$

$$\mathbf{A}_p = \mathbf{b}_p + \hat{\mathbf{z}} \times \int_z^{z_2} \mathbf{P} dz', \quad (\text{A2})$$

where $\mathbf{b} = \mathbf{b}_p \equiv \bar{\mathbf{b}}$ is a particular solution specified and proved by Valori et al. (2012) as follows:

$$\bar{b}_x = -\frac{1}{2} \int_{y_1}^y B_z(x, y', z_2) dy', \quad (\text{A3})$$

$$\bar{b}_y = \frac{1}{2} \int_{x_1}^x B_z(x', y, z_2) dx'. \quad (\text{A4})$$

Equations (A1) – (A4) is a performable scheme for deriving vector potential before computing helicity with FV method. The method as carried out above estimates a global quantity of magnetic helicity. Moreover, one could refer to the relative field line helicity (e.g., Yeates & Page 2018; Moraitis et al. 2019a, 2021), which is developing vigorously in recent years, for a distribution investigation.

REFERENCES

- Amari, T., Boulmezaoud, T. Z., & Aly, J. J. 2006, *A&A*, 446, 691, doi: [10.1051/0004-6361:20054076](https://doi.org/10.1051/0004-6361:20054076)
- Aschwanden, M. J. 2019, *ApJ*, 874, 131, doi: [10.3847/1538-4357/ab0b42](https://doi.org/10.3847/1538-4357/ab0b42)
- Awasthi, A. K., Liu, R., Wang, H., Wang, Y., & Shen, C. 2018, *ApJ*, 857, 124, doi: [10.3847/1538-4357/aab7fb](https://doi.org/10.3847/1538-4357/aab7fb)
- Bateman, G. 1978, *MHD instabilities*
- Baty, H. 2001, *A&A*, 367, 321, doi: [10.1051/0004-6361:20000412](https://doi.org/10.1051/0004-6361:20000412)
- Bennett, K., Roberts, B., & Narain, U. 1999, *SoPh*, 185, 41, doi: [10.1023/A:1005141432432](https://doi.org/10.1023/A:1005141432432)
- Berger, M. A. 1999, *Plasma Physics and Controlled Fusion*, 41, B167, doi: [10.1088/0741-3335/41/12B/312](https://doi.org/10.1088/0741-3335/41/12B/312)
- . 2003, in *Advances in Nonlinear Dynamics*, ed. A. Ferriz-Mas & M. Núñez, 345–374, doi: [10.1201/9780203493137.ch10](https://doi.org/10.1201/9780203493137.ch10)
- Berger, M. A., & Asgari-Targhi, M. 2009, *ApJ*, 705, 347, doi: [10.1088/0004-637X/705/1/347](https://doi.org/10.1088/0004-637X/705/1/347)
- Berger, M. A., & Field, G. B. 1984, *Journal of Fluid Mechanics*, 147, 133, doi: [10.1017/S0022112084002019](https://doi.org/10.1017/S0022112084002019)
- Berger, M. A., & Prior, C. 2006, *Journal of Physics A Mathematical General*, 39, 8321, doi: [10.1088/0305-4470/39/26/005](https://doi.org/10.1088/0305-4470/39/26/005)
- Bobra, M. G., Sun, X., Hoeksema, J. T., et al. 2014, *SoPh*, 289, 3549, doi: [10.1007/s11207-014-0529-3](https://doi.org/10.1007/s11207-014-0529-3)
- Borrero, J. M., & Ichimoto, K. 2011, *Living Reviews in Solar Physics*, 8, 4, doi: [10.12942/lrsp-2011-4](https://doi.org/10.12942/lrsp-2011-4)
- Brown, D., & Walker, A. 2021, *SoPh*, 296, 48, doi: [10.1007/s11207-021-01787-4](https://doi.org/10.1007/s11207-021-01787-4)
- Brueckner, G. E., Howard, R. A., Koomen, M. J., et al. 1995, *SoPh*, 162, 357, doi: [10.1007/BF00733434](https://doi.org/10.1007/BF00733434)
- Cao, W., Goode, P. R., Ahn, K., et al. 2012, in *Astronomical Society of the Pacific Conference Series*, Vol. 463, Second ATST-EAST Meeting: Magnetic Fields from the Photosphere to the Corona., ed. T. R. Rimmele, A. Tritschler, F. Wöger, M. Collados Vera, H. Socas-Navarro, R. Schlichenmaier, M. Carlsson, T. Berger, A. Cadavid, P. R. Gilbert, P. R. Goode, & M. Knölker, 291
- Chandra, R., Schmieder, B., Mandrini, C. H., et al. 2011, *SoPh*, 269, 83, doi: [10.1007/s11207-010-9670-9](https://doi.org/10.1007/s11207-010-9670-9)
- Chen, J. 1996, *J. Geophys. Res.*, 101, 27499, doi: [10.1029/96JA02644](https://doi.org/10.1029/96JA02644)
- Chen, P. F. 2011, *Living Reviews in Solar Physics*, 8, 1, doi: [10.12942/lrsp-2011-1](https://doi.org/10.12942/lrsp-2011-1)
- Cheng, X., & Ding, M. D. 2016, *ApJS*, 225, 16, doi: [10.3847/0067-0049/225/1/16](https://doi.org/10.3847/0067-0049/225/1/16)
- Cheng, X., Ding, M. D., & Fang, C. 2015, *ApJ*, 804, 82, doi: [10.1088/0004-637X/804/2/82](https://doi.org/10.1088/0004-637X/804/2/82)
- Cheng, X., Ding, M. D., Zhang, J., et al. 2014, *ApJ*, 789, 93, doi: [10.1088/0004-637X/789/2/93](https://doi.org/10.1088/0004-637X/789/2/93)
- Cheung, M. C. M., Rempel, M., Chintzoglou, G., et al. 2019, *Nature Astronomy*, 3, 160, doi: [10.1038/s41550-018-0629-3](https://doi.org/10.1038/s41550-018-0629-3)
- Chiu, Y. T., & Hilton, H. H. 1977, *ApJ*, 212, 873, doi: [10.1086/155111](https://doi.org/10.1086/155111)
- Cirtain, J. W., Golub, L., Winebarger, A. R., et al. 2013, *Nature*, 493, 501, doi: [10.1038/nature11772](https://doi.org/10.1038/nature11772)
- De Pontieu, B., Title, A. M., Lemen, J. R., et al. 2014, *SoPh*, 289, 2733, doi: [10.1007/s11207-014-0485-y](https://doi.org/10.1007/s11207-014-0485-y)
- Demoulin, P., Henoux, J. C., Priest, E. R., & Mandrini, C. H. 1996, *A&A*, 308, 643
- DeVore, C. R. 2000, *ApJ*, 539, 944, doi: [10.1086/309274](https://doi.org/10.1086/309274)
- DeVore, C. R., & Antiochos, S. K. 2000, *ApJ*, 539, 954, doi: [10.1086/309275](https://doi.org/10.1086/309275)
- Domingo, V., Fleck, B., & Poland, A. I. 1995, *SoPh*, 162, 1, doi: [10.1007/BF00733425](https://doi.org/10.1007/BF00733425)
- Duan, A., Jiang, C., He, W., et al. 2019, *ApJ*, 884, 73, doi: [10.3847/1538-4357/ab3e33](https://doi.org/10.3847/1538-4357/ab3e33)
- Duan, A., Jiang, C., Hu, Q., et al. 2017, *ApJ*, 842, 119, doi: [10.3847/1538-4357/aa76e1](https://doi.org/10.3847/1538-4357/aa76e1)
- Duan, A., Jiang, C., Zou, P., Feng, X., & Cui, J. 2021, *ApJ*, 906, 45, doi: [10.3847/1538-4357/abc701](https://doi.org/10.3847/1538-4357/abc701)
- Dungey, J. W., & Loughhead, R. E. 1954, *Australian Journal of Physics*, 7, 5, doi: [10.1071/PH540005](https://doi.org/10.1071/PH540005)
- Finn, J. M., & Antonsen, Thomas M., J. 1985, *Comments on Plasma Physics and Controlled Fusion*, 9, 111
- Gary, G. A. 2001, *SoPh*, 203, 71, doi: [10.1023/A:1012722021820](https://doi.org/10.1023/A:1012722021820)
- Gilchrist, S. A., & Wheatland, M. S. 2014, *SoPh*, 289, 1153, doi: [10.1007/s11207-013-0406-5](https://doi.org/10.1007/s11207-013-0406-5)
- Gopalswamy, N., Yashiro, S., Michalek, G., et al. 2009, *Earth Moon and Planets*, 104, 295, doi: [10.1007/s11038-008-9282-7](https://doi.org/10.1007/s11038-008-9282-7)
- Grad, H., & Rubin, H. 1958, in *Proc. 2nd Int. Conf., Peaceful Uses of Atomic Energy*, 31: Theoretical and Experimental Aspects of Controlled Nuclear Fusion, ed. J. H. Martens et al. (Geneva: United Nations), 190
- Guo, J. H., Ni, Y. W., Qiu, Y., et al. 2021, *ApJ*, 917, 81, doi: [10.3847/1538-4357/ac0cef](https://doi.org/10.3847/1538-4357/ac0cef)
- Guo, Y., Cheng, X., & Ding, M. 2017a, *Science China Earth Sciences*, 60, 1408, doi: [10.1007/s11430-017-9081-x](https://doi.org/10.1007/s11430-017-9081-x)
- Guo, Y., Ding, M. D., Cheng, X., Zhao, J., & Pariat, E. 2013, *ApJ*, 779, 157, doi: [10.1088/0004-637X/779/2/157](https://doi.org/10.1088/0004-637X/779/2/157)
- Guo, Y., Ding, M. D., Schmieder, B., et al. 2010, *ApJL*, 725, L38, doi: [10.1088/2041-8205/725/1/L38](https://doi.org/10.1088/2041-8205/725/1/L38)
- Guo, Y., Xia, C., Keppens, R., & Valori, G. 2016, *ApJ*, 828, 82, doi: [10.3847/0004-637X/828/2/82](https://doi.org/10.3847/0004-637X/828/2/82)

- Guo, Y., Pariat, E., Valori, G., et al. 2017b, *ApJ*, 840, 40, doi: [10.3847/1538-4357/aa6aa8](https://doi.org/10.3847/1538-4357/aa6aa8)
- Gupta, M., Thalmann, J. K., & Veronig, A. M. 2021, *A&A*, 653, A69, doi: [10.1051/0004-6361/202140591](https://doi.org/10.1051/0004-6361/202140591)
- Harvey, J. W. 2012, *SoPh*, 280, 69, doi: [10.1007/s11207-012-0067-9](https://doi.org/10.1007/s11207-012-0067-9)
- Hoeksema, J. T., Liu, Y., Hayashi, K., et al. 2014, *SoPh*, 289, 3483, doi: [10.1007/s11207-014-0516-8](https://doi.org/10.1007/s11207-014-0516-8)
- Hood, A. W., & Priest, E. R. 1979, *SoPh*, 64, 303, doi: [10.1007/BF00151441](https://doi.org/10.1007/BF00151441)
- . 1981, *Geophysical and Astrophysical Fluid Dynamics*, 17, 297, doi: [10.1080/03091928108243687](https://doi.org/10.1080/03091928108243687)
- Hu, Q., & Dasgupta, B. 2008, *SoPh*, 247, 87, doi: [10.1007/s11207-007-9090-7](https://doi.org/10.1007/s11207-007-9090-7)
- Hu, Q., Dasgupta, B., Derosa, M. L., Büchner, J., & Gary, G. A. 2010, *Journal of Atmospheric and Solar-Terrestrial Physics*, 72, 219, doi: [10.1016/j.jastp.2009.11.014](https://doi.org/10.1016/j.jastp.2009.11.014)
- Hu, Q., Qiu, J., Dasgupta, B., Khare, A., & Webb, G. M. 2014, *ApJ*, 793, 53, doi: [10.1088/0004-637X/793/1/53](https://doi.org/10.1088/0004-637X/793/1/53)
- James, A. W., Valori, G., Green, L. M., et al. 2018, *ApJL*, 855, L16, doi: [10.3847/2041-8213/aab15d](https://doi.org/10.3847/2041-8213/aab15d)
- Jiang, C., & Feng, X. 2012, *ApJ*, 749, 135, doi: [10.1088/0004-637X/749/2/135](https://doi.org/10.1088/0004-637X/749/2/135)
- . 2013, *ApJ*, 769, 144, doi: [10.1088/0004-637X/769/2/144](https://doi.org/10.1088/0004-637X/769/2/144)
- Jiang, C., Wu, S. T., Feng, X., & Hu, Q. 2014, *ApJ*, 780, 55, doi: [10.1088/0004-637X/780/1/55](https://doi.org/10.1088/0004-637X/780/1/55)
- Jiang, C., Feng, X., Liu, R., et al. 2021, *Nature Astronomy*, 5, 1126, doi: [10.1038/s41550-021-01414-z](https://doi.org/10.1038/s41550-021-01414-z)
- Jin, C. L., Harvey, J. W., & Pietarila, A. 2013, *ApJ*, 765, 79, doi: [10.1088/0004-637X/765/2/79](https://doi.org/10.1088/0004-637X/765/2/79)
- Kilpua, E. K. J., Pomoell, J., Price, D., Sarkar, R., & Asvestari, E. 2021, *Frontiers in Astronomy and Space Sciences*, 8, 35, doi: [10.3389/fspas.2021.631582](https://doi.org/10.3389/fspas.2021.631582)
- Kliem, B., & Török, T. 2006, *PhRvL*, 96, 255002, doi: [10.1103/PhysRevLett.96.255002](https://doi.org/10.1103/PhysRevLett.96.255002)
- Lagg, A., Lites, B., Harvey, J., Gosain, S., & Centeno, R. 2017, *SSRv*, 210, 37, doi: [10.1007/s11214-015-0219-y](https://doi.org/10.1007/s11214-015-0219-y)
- Lee, H., & Magara, T. 2018, *ApJ*, 859, 132, doi: [10.3847/1538-4357/aabfe6](https://doi.org/10.3847/1538-4357/aabfe6)
- Leenaarts, J., Carlsson, M., & Rouppe van der Voort, L. 2015, *ApJ*, 802, 136, doi: [10.1088/0004-637X/802/2/136](https://doi.org/10.1088/0004-637X/802/2/136)
- Lemen, J. R., Title, A. M., Akin, D. J., et al. 2012, *SoPh*, 275, 17, doi: [10.1007/s11207-011-9776-8](https://doi.org/10.1007/s11207-011-9776-8)
- Linan, L., Pariat, E., Moraitis, K., Valori, G., & Leake, J. 2018, *ApJ*, 865, 52, doi: [10.3847/1538-4357/aadae7](https://doi.org/10.3847/1538-4357/aadae7)
- Liu, R., Kliem, B., Titov, V. S., et al. 2016, *ApJ*, 818, 148, doi: [10.3847/0004-637X/818/2/148](https://doi.org/10.3847/0004-637X/818/2/148)
- Low, B. C. 1991, *ApJ*, 370, 427, doi: [10.1086/169829](https://doi.org/10.1086/169829)
- . 1992, *ApJ*, 399, 300, doi: [10.1086/171925](https://doi.org/10.1086/171925)
- Mandrini, C. H., Demoulin, P., Schmieder, B., et al. 2006, *SoPh*, 238, 293, doi: [10.1007/s11207-006-0205-3](https://doi.org/10.1007/s11207-006-0205-3)
- McKenzie, D. E., & Canfield, R. C. 2008, *A&A*, 481, L65, doi: [10.1051/0004-6361:20079035](https://doi.org/10.1051/0004-6361:20079035)
- Moffatt, H. K., & Ricca, R. L. 1992, *Proceedings of the Royal Society of London Series A*, 439, 411, doi: [10.1098/rspa.1992.0159](https://doi.org/10.1098/rspa.1992.0159)
- Moraitis, K., Pariat, E., Valori, G., & Dalmasse, K. 2019a, *A&A*, 624, A51, doi: [10.1051/0004-6361/201834668](https://doi.org/10.1051/0004-6361/201834668)
- Moraitis, K., Patsourakos, S., & Nindos, A. 2021, *A&A*, 649, A107, doi: [10.1051/0004-6361/202140384](https://doi.org/10.1051/0004-6361/202140384)
- Moraitis, K., Sun, X., Pariat, E., & Linan, L. 2019b, *A&A*, 628, A50, doi: [10.1051/0004-6361/201935870](https://doi.org/10.1051/0004-6361/201935870)
- Pariat, E., Leake, J. E., Valori, G., et al. 2017, *A&A*, 601, A125, doi: [10.1051/0004-6361/201630043](https://doi.org/10.1051/0004-6361/201630043)
- Parker, E. N. 1983, *ApJ*, 264, 642, doi: [10.1086/160637](https://doi.org/10.1086/160637)
- Pesnell, W. D., Thompson, B. J., & Chamberlin, P. C. 2012, *SoPh*, 275, 3, doi: [10.1007/s11207-011-9841-3](https://doi.org/10.1007/s11207-011-9841-3)
- Pontin, D. I., Janvier, M., Tiwari, S. K., et al. 2017, *ApJ*, 837, 108, doi: [10.3847/1538-4357/aa5ff9](https://doi.org/10.3847/1538-4357/aa5ff9)
- Priest, E. 2014, *Magnetohydrodynamics of the Sun*, doi: [10.1017/CBO9781139020732](https://doi.org/10.1017/CBO9781139020732)
- Sakurai, T. 1982, *SoPh*, 76, 301, doi: [10.1007/BF00170988](https://doi.org/10.1007/BF00170988)
- . 1989, *SSRv*, 51, 11, doi: [10.1007/BF00226267](https://doi.org/10.1007/BF00226267)
- Savcheva, A., Pariat, E., McKillop, S., et al. 2016, *ApJ*, 817, 43, doi: [10.3847/0004-637X/817/1/43](https://doi.org/10.3847/0004-637X/817/1/43)
- Schou, J., Scherrer, P. H., Bush, R. I., et al. 2012, *SoPh*, 275, 229, doi: [10.1007/s11207-011-9842-2](https://doi.org/10.1007/s11207-011-9842-2)
- Shen, J., Ji, H., & Su, Y. 2022, *Research in Astronomy and Astrophysics*, 22, 015019, doi: [10.1088/1674-4527/ac389b](https://doi.org/10.1088/1674-4527/ac389b)
- Solanki, S. K., Inhester, B., & Schüssler, M. 2006, *Reports on Progress in Physics*, 69, 563, doi: [10.1088/0034-4885/69/3/R02](https://doi.org/10.1088/0034-4885/69/3/R02)
- Su, Y. 2019, *ChA&A*, 43, 305, doi: [10.1016/j.chinastron.2018.09.011](https://doi.org/10.1016/j.chinastron.2018.09.011)
- Sun, X. 2013, *arXiv e-prints*, arXiv:1309.2392. <https://arxiv.org/abs/1309.2392>
- Sun, X., Török, T., & DeRosa, M. L. 2022, *MNRAS*, 509, 5075, doi: [10.1093/mnras/stab3249](https://doi.org/10.1093/mnras/stab3249)
- Swarztrauber, P. N., & Sweet, R. A. 1979, *ACM Trans. Math. Softw*, 5, 352, doi: [10.1145/355841.355850](https://doi.org/10.1145/355841.355850)
- Thalmann, J. K., Moraitis, K., Linan, L., et al. 2019, *ApJ*, 887, 64, doi: [10.3847/1538-4357/ab4e15](https://doi.org/10.3847/1538-4357/ab4e15)
- Thalmann, J. K., Georgoulis, M. K., Liu, Y., et al. 2021, *ApJ*, 922, 41, doi: [10.3847/1538-4357/ac1f93](https://doi.org/10.3847/1538-4357/ac1f93)
- Titov, V. S., & Démoulin, P. 1999, *A&A*, 351, 707
- Titov, V. S., Hornig, G., & Démoulin, P. 2002, *Journal of Geophysical Research (Space Physics)*, 107, 1164, doi: [10.1029/2001JA000278](https://doi.org/10.1029/2001JA000278)

- Tiwari, S. K. 2012, *ApJ*, 744, 65,
doi: [10.1088/0004-637X/744/1/65](https://doi.org/10.1088/0004-637X/744/1/65)
- Toriumi, S., & Park, S.-H. 2022, arXiv e-prints,
arXiv:2204.06010. <https://arxiv.org/abs/2204.06010>
- Török, T., Kliem, B., & Titov, V. S. 2004, *A&A*, 413, L27,
doi: [10.1051/0004-6361:20031691](https://doi.org/10.1051/0004-6361:20031691)
- Valori, G., Démoulin, P., & Pariat, E. 2012, *SoPh*, 278, 347,
doi: [10.1007/s11207-012-9951-6](https://doi.org/10.1007/s11207-012-9951-6)
- Valori, G., Kliem, B., & Fuhrmann, M. 2007, *SoPh*, 245,
263, doi: [10.1007/s11207-007-9046-y](https://doi.org/10.1007/s11207-007-9046-y)
- Valori, G., Pariat, E., Anfinogentov, S., et al. 2016, *SSRv*,
201, 147, doi: [10.1007/s11214-016-0299-3](https://doi.org/10.1007/s11214-016-0299-3)
- van Ballegooijen, A. A. 2004, *ApJ*, 612, 519,
doi: [10.1086/422512](https://doi.org/10.1086/422512)
- Vemareddy, P., Cheng, X., & Ravindra, B. 2016, *ApJ*, 829,
24, doi: [10.3847/0004-637X/829/1/24](https://doi.org/10.3847/0004-637X/829/1/24)
- Vemareddy, P., & Zhang, J. 2014, *ApJ*, 797, 80,
doi: [10.1088/0004-637X/797/2/80](https://doi.org/10.1088/0004-637X/797/2/80)
- Wang, Y., Zhuang, B., Hu, Q., et al. 2016, *Journal of
Geophysical Research (Space Physics)*, 121, 9316,
doi: [10.1002/2016JA023075](https://doi.org/10.1002/2016JA023075)
- Wang, Y., Shen, C., Liu, R., et al. 2018, *Journal of
Geophysical Research (Space Physics)*, 123, 3238,
doi: [10.1002/2017JA024971](https://doi.org/10.1002/2017JA024971)
- Wheatland, M. S., Sturrock, P. A., & Roumeliotis, G. 2000,
ApJ, 540, 1150, doi: [10.1086/309355](https://doi.org/10.1086/309355)
- Wiegelmann, T. 2004, *SoPh*, 219, 87,
doi: [10.1023/B:SOLA.0000021799.39465.36](https://doi.org/10.1023/B:SOLA.0000021799.39465.36)
- . 2008, *Journal of Geophysical Research (Space Physics)*,
113, A03S02, doi: [10.1029/2007JA012432](https://doi.org/10.1029/2007JA012432)
- Wiegelmann, T., Petrie, G. J. D., & Riley, P. 2017, *SSRv*,
210, 249, doi: [10.1007/s11214-015-0178-3](https://doi.org/10.1007/s11214-015-0178-3)
- Wiegelmann, T., & Sakurai, T. 2021, *Living Reviews in
Solar Physics*, 18, 1, doi: [10.1007/s41116-020-00027-4](https://doi.org/10.1007/s41116-020-00027-4)
- Wiegelmann, T., Thalmann, J. K., Schrijver, C. J., De
Rosa, M. L., & Metcalf, T. R. 2008, *SoPh*, 247, 249,
doi: [10.1007/s11207-008-9130-y](https://doi.org/10.1007/s11207-008-9130-y)
- Wiegelmann, T., Xia, L. D., & Marsch, E. 2005, *A&A*, 432,
L1, doi: [10.1051/0004-6361:200500029](https://doi.org/10.1051/0004-6361:200500029)
- Yeates, A. R., & Page, M. H. 2018, *Journal of Plasma
Physics*, 84, 775840602, doi: [10.1017/S0022377818001204](https://doi.org/10.1017/S0022377818001204)
- Zhang, J., Cheng, X., & Ding, M.-D. 2012, *Nature
Communications*, 3, 747, doi: [10.1038/ncomms1753](https://doi.org/10.1038/ncomms1753)
- Zhang, J., Temmer, M., Gopalswamy, N., et al. 2021,
Progress in Earth and Planetary Science, 8, 56,
doi: [10.1186/s40645-021-00426-7](https://doi.org/10.1186/s40645-021-00426-7)
- Zhang, P., Chen, J., Liu, R., & Wang, C. 2022, *ApJ*, 937,
26, doi: [10.3847/1538-4357/ac8d61](https://doi.org/10.3847/1538-4357/ac8d61)
- Zhao, J., Gilchrist, S. A., Aulanier, G., et al. 2016, *ApJ*,
825, 80, doi: [10.3847/0004-637X/825/1/80](https://doi.org/10.3847/0004-637X/825/1/80)
- Zhao, J., Li, H., Pariat, E., et al. 2014, *ApJ*, 787, 88,
doi: [10.1088/0004-637X/787/1/88](https://doi.org/10.1088/0004-637X/787/1/88)
- Zhao, J., Schmieder, B., Li, H., et al. 2017, *ApJ*, 836, 52,
doi: [10.3847/1538-4357/836/1/52](https://doi.org/10.3847/1538-4357/836/1/52)
- Zhong, Z., Guo, Y., & Ding, M. D. 2021, *Nature
Communications*, 12, 2734,
doi: [10.1038/s41467-021-23037-8](https://doi.org/10.1038/s41467-021-23037-8)
- Zhou, G. P., Zhang, J., & Wang, J. X. 2016, *ApJL*, 823,
L19, doi: [10.3847/2041-8205/823/1/L19](https://doi.org/10.3847/2041-8205/823/1/L19)
- Zhu, X., Neukirch, T., & Wiegelmann, T. 2022, *Sci China
Tech Sci*, 65, doi: [10.1007/s11431-022-2047-8](https://doi.org/10.1007/s11431-022-2047-8)
- Zhu, X., Wang, H., Du, Z., & He, H. 2016, *ApJ*, 826, 51,
doi: [10.3847/0004-637X/826/1/51](https://doi.org/10.3847/0004-637X/826/1/51)
- Zhu, X., & Wiegelmann, T. 2018, *ApJ*, 866, 130,
doi: [10.3847/1538-4357/aadf7f](https://doi.org/10.3847/1538-4357/aadf7f)
- . 2019, *A&A*, 631, A162,
doi: [10.1051/0004-6361/201936433](https://doi.org/10.1051/0004-6361/201936433)
- . 2022, *A&A*, 658, A37,
doi: [10.1051/0004-6361/202141505](https://doi.org/10.1051/0004-6361/202141505)
- Zhu, X., Wiegelmann, T., & Solanki, S. K. 2020, *A&A*, 640,
A103, doi: [10.1051/0004-6361/202037766](https://doi.org/10.1051/0004-6361/202037766)
- Zuccarello, F. P., Pariat, E., Valori, G., & Linan, L. 2018,
ApJ, 863, 41, doi: [10.3847/1538-4357/aacdfc](https://doi.org/10.3847/1538-4357/aacdfc)